Synthesis of Surfactant-Mediated Direct Band-Gap Tunable $(CdS)_x(CdCl_2)_y$ Nanocomposites

C. O'Dwyer, [a,*] V. Lavayen, [a,b] N. Mirabal, [b] M. A. Santa Ana, [c] E. Benavente, [b] S. Ormazabal, [c] G. González, [c] Z. Lopez, [c] O. Schöps, [d] S. B. Newcomb, [e] U. Woggon, [d] C. M. Sotomayor Torres [a]

[a] *Tyndall National Institute, University College Cork, Cork, Ireland*

[b] *Department of Chemistry, Universidad Tecnológica Metropolitana, P.O Box 9845, Santiago, Chile*

[c] *Department of Chemistry, Faculty of Science, Universidad de Chile, P. O. Box 653, Santiago, Chile*

[d] *Fachbereich Physik, Universität Dortmund, Otto-Hahn-Strasse 4, 44227 Dortmund, Germany*

[e] *Glebe Scientific Ltd., Newport, Co. Tipperary, Ireland*

Abstract

The optical-structural characteristics of the direct optical band-gap semiconducting series of surfactant template-mediated laminar $(CdS)_x(CdCl_2)_y(C_nH_{2n+4}N)_z$ nanocomposites are reported. X-ray diffraction measurements of the nanocomposites exhibited interlaminar distances in the range 0.29−0.36 nm with observations of eighth order $\{00l\}$ diffraction planes indicative of a high degree of laminarity and crystallographic order. Diffuse reflectance measurements have determined that the profile of their emission spectrum is that of a direct band-gap with absorption edges in the range 2.11−2.40 eV, depending on the CdS mole fraction in the nanocomposite. Photoluminescence (PL) excitation and time-resolved PL spectroscopies give an estimate of the maximum relative absorbance of the nanocomposites at ∼420 nm while the minimum was observed at ∼560 nm. The main emission was observed at ∼670 nm with emission from doubly ionized sulphur vacancies observed at ∼615 nm at room temperature. The concomitant formation of semiconducting CdS renders this modular system amenable for tuned optical emission.

Key words: Cadmium sulphide, Scanning electron microscopy, Photoluminescence, Optical properties, Nanostructures

1 Introduction

The technological implications for the design and manufacture of new classes of optoelectronic and electronic devices together with the associated emergence of new physics, have resulted in this field being one of the most active in nanoscale science and technology today [1]. Obtaining new nanomaterials through simple chemical synthesis routes that have controllable and tunable optical properties is an obvious necessity in the realization of photonically functional nanoscale structures and devices. The study of guest-molecule intercalation among the lamina of the host compound has been gaining increased consideration for several reasons. Among those are the modifications and controllability of the optical and electronic properties of the compound obtained [2]. The advantages of the rapidly developing organic light-emitting diode (OLED) technology [3] can be combined with attractive properties of semiconductor nanocrystals. Optical properties of this class of lumophores are determined by the quantum confinement effect [4], so that their emission colour and the electron affinity can be finely controlled not only by the material choice but also by size within a single synthetic route.

A remarkable number of crystalline inorganic compounds with laminar characteristics, such as some transition metal oxides, are well known due to several of their chemical properties, with emphasis on their ion exchange, intercalation and polarization properties. These matrices can accommodate simple ions, relatively large ionic species, organic molecules or organic ions and coordination with organometallic compounds [5].

Due to high efficiency, simplicity and versatility of their synthesis, bottom-up approaches using surfactants or micelles as the regulating structural agents or templates are readily employed in the fabrication of one-dimensional nanostructures [6]. In particular, II−IV semiconductor compounds such as cadmium disulfide, for example, which has a direct optical band-gap of $E_g = 2.42$ eV at room temperature, are widely used for optoelectronic devices [7] and in the study of optically active nanoparticles. Recent reports have shown the formation of particles using zeolites as a structural matrix [8], polymeric matrices [9], as well as CdS nanocrystals embedded in surfactant-water emulsions [5], nanowires [1], and nanohelices [11,12]. State-of-the-art syntheses, which can be carried out either in organic solvents [13] or in water [14], provide different II-VI and III-V nanocrystals with variable size and a narrow size distribution leading to narrow emission spectra: 25−35 nm full width at half maximum (FWHM) in solution, tunable from the UV to the near-IR spectral region [15].

* Corresponding author. Tel: + 353 21 490-4391; Fax: + 353 21 490-4467.
Email address: codwyer@tyndall.ie (C. O'Dwyer,).

This work reports the synthesis and optical-structural characteristics of a tunable direct optical band-gap semiconducting series of surfactant template-mediated laminar $(CdS)_x(CdCl_2)_y(C_nH_{2n+4}N)_z$ nanocomposites. Because surface state modifications of size-quantized semiconductor particles have been shown to result in markedly altered band-gaps, flat-band potentials, and electron and hole trapping rates [16,17], new syntheses offer the possibility of tailoring electron and photoelectron transfers to desired energy levels and thus a new approach in controlling the light-emitting properties and energy transfer using intercalation chemistry.

2 Experimental

2.1 Synthesis of Surfactant-Mediated $(CdS)_x(CdCl_2)_y(C_nH_{2n+4}N)_z$ Nanocomposites

As-received antimony disulfide powder (Merck), hexacetyltrimethylammoniun bromide (CTAB) 97%, cadmium chloride (Matheson Coleman & Bell), and octacetyltrimethylammoniun bromide (OTAB) 97%, were employed for the synthesis of the nanocomposites. Water was twice distilled and carefully degassed under argon bubbling. Several groups of compounds were synthesised as outlined below.

$CdCl_2$-CTAB (A1C) and $CdCl_2$-OTAB (A2O)
The $CdCl_2$-CTAB (A1C) complex was synthesized by preparing a surfactant gel using CTAB. The molar ratio CTAB:H_2O was 1:24 or 84% (w/w). The suspension underwent vigorous stirring at a temperature of 333 K for 24 h. The $CdCl_2$-OTAB (A2O) was prepared using an OTAB gel following the same procedure. The resulting white solid products were then washed in ethanol, centrifuged and dried in an argon atmosphere.

CdS_x-CTAB (A1) and CdS_x-OTAB (A2)
The CdS_x-CTAB (A1) and CdS_x-OTAB (A2) laminar nanocomposites were prepared by adding a $CdCl_2$-ethanol solution with a concentration of 0.05 mol dm^{-3} to the surfactant gel outlined above in a H_2S atmosphere. The composition was calculated considering a final molar ratio $CdCl_2$:surfactant of 1:2 (w/w). The reaction was kept at room temperature under constant stirring for a period of 16 h. During this period the flow rate volume of the H_2S was 362 scmm. Finally, the yellow solid product was washed in ethanol, centrifuged and dried in an argon atmosphere. The gaseous H_2S was obtained using iron (II) sulphide and concentrated HCl as precursors according to:

$$FeS(s) + 2HCl(l) \rightarrow H_2S(g) + FeCl_2(s) \quad (1)$$

The concentration of the ethanolic solution of the H_2S was determined by titrating against a standard solution of 0.1 N NaOH and phenolphthalein as the *p*H indicator.

CdS_x-CTAB (75-100)
A suspension of CTAB and deionised water with a molar ratio of CTAB:H_2O of 1:25 was prepared. Subsequently, a 300 ml ethanolic solution containing H_2S (0.27 mol dm^{-3}) was added to the CTAB aqueous suspension under constant stirring at room temperature for a period of 2 h. The next step involved the addition of 75 ml of solution containing CTAB-H_2S to 100 ml of an ethanolic solution of $CdCl_2$ with an initial concentration of 0.057 mol dm^{-3}. The reaction was maintained for a period of 16 h under constant stirring at room temperature. The yellow product was washed with ethanol, centrifuged and storage in vacuum.

CdS_x-OTAB (1:8) and CdS_x-OTAB (1:10)
A suspension of OTAB and deionised water with a molar ratio of OTAB:H_2O of 1:25 was prepared. Subsequently, a 300 ml ethanolic solution containing H_2S (0.27 mol dm^{-3}) was added to the OTAB aqueous suspension under constant stirring at room temperature for a period of 1 h. The sulphurous surfactant-containing aqueous solution was added to a 0.05 mol dm^{-3} ethanolic $CdCl_2$ solution under vigorous stirring for a period of 16 h at room temperature to produce a yellow suspension. The volume of the final suspension was calculated to obtain a final $CdCl_2$:H_2S molar ratio of 1:8 and 1:10 for the CdS_x-OTAB (1:8) and CdS_x-OTAB (1:10) laminar nanocomposites, respectively. The final products were light-yellow suspensions that were washed in ethanol, centrifuged and stored in vacuum. The same procedure was used to obtain similarly stoichiometric nanocomposites using CTAB.

CdS_x-CTAB (C1) and CdS_x-OTAB (C2)
Each of the $CdCl_2$ complexes were mixed with 80 ml of an ethanolic solution of H_2S (0.27 mol dm^{-3}) for a period of 16 h at room temperature. The products were yellow suspensions that were centrifuged, washed with ethanol and stored in vacuum. The CdS_x-CTAB (C1) product obtained contained CTAB and the CdS_x-OTAB (C2) the OTAB ammonium salt.

2.2 Characterization of Samples

X-ray powder diffraction characterization was performed using a SIEMENS D5000 diffractometer (Cu-K_α, $\lambda = 1.5418$ Å, operation voltage 40 kV, current 30 mA). The morphology of the laminar nanocomposite was examined by scanning electron microscopy (SEM) using a JEOL JSM-6700F field-emission SEM operating at beam voltages between 1-10 kV. Atomic force microscopy (AFM)

was conducted on selected samples using a Veeco Nanoscope IIIa Multi-Mode in tapping mode. Electron transparent specimens were prepared by ion-milling techniques and placed on a holey carbon support. Transmission electron microscopy (TEM) and electron diffraction (ED) were conducted using a JEOL 2000FX operating at 200 kV. The chemical compositions of the samples were determined by elemental chemical analysis (SISONS Model EA-1108) and atomic absorption spectrometry (UNICAM 929).

The diffuse reflectance spectra (DRS) were acquired Shimadzu UV/VIS/NIR spectrophotometer with an integrating sphere in the range 1.55−3.4 eV. White light from a tungsten lamp was focused onto the sample through an optical microscope. The diffuse reflectance signal was then collected by a photomultiplier using a double monochromator and lock-in amplifier.

For the photoluminescence (PL) measurements, samples were embedded between two 0.1 mm glass cover slips. All measurements were performed at room temperature. The excitation light source used was a Xe Lamp (Osram XBO 150), spectrally filtered with a 1 m monochromator (spectral resolution 1 nm) yielding a wavelength dependent excitation intensity in the mW cm^{-2} range. For higher power excitation a Nd:YAG laser (*Verdi* by Coherent) was used operating at 532 nm. The attenuation and focusing onto the sample resulted in an excitation intensity in the range 0.4−4000 W cm^{-2}. Alternatively a GaInN laser (*Vioflame* by Coherent) was used, operating at 409 nm with excitation intensities in the range 0.3−1000 W cm^{-2}. The excitation light was focused onto the sample with a $f = 90$ mm achromatic lens. Luminescence is collected with a $f = 60$ mm achromat. In the case of laser excitation a high-pass filter (Schott OG570) was used to suppress scattered excitation light. The luminescence was imaged onto the entrance slit of a 0.25 m spectrometer (resolution 0.7 nm) with an optical multichannel analyser (OMA), intensified with a multichannel plate, as the detector in the wavelength range 400−850 nm. For the PLE measurements the excitation intensity is monitored by a photo diode that detects a fraction of the light emanating from the monochromator. The output is amplified (60 dB) and sampled with a 12 bit A/D converter. From this data the incident photon flux is calculated and used for normalization.

3 Results and Discussion

3.1 Structure of the $(CdS)_x(CdCl_2)_y(C_nH_{2n+4}N)_z$ Nanocomposites

The structure and morphology of the synthesised nanocomposites were analysed by FESEM. Typical micrographs of the CdS_x-CTAB (75-100) and CdS_x-OTAB (1:8) nanocomposites are shown in Fig. 1. It is apparent from the

micrographs that the overall morphology is that of a bulk laminar compound. Similar morphological characteristics were noted for all nanocomposites described in this work.

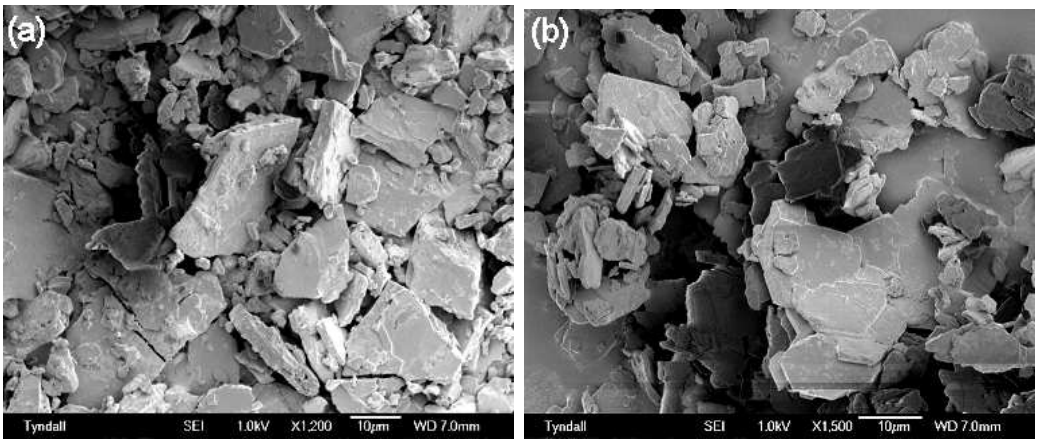

Fig. 1. SEM images of (a) CdS_x-CTAB (75-100) and (b) CdS_x-OTAB (1:8) nanocomposites.

Higher magnification micrographs of the CdS_x-CTAB (75-100) nanocomposite were acquired and a typical image is shown in Fig. 2a. The laminarity of this layered compound is apparent from the tilted cross-section. AFM was employed to characterise the outermost surface of the bulk lamina. A 250 nm $\times$ 250 nm AFM image of the region of surface highlighted in Fig. 2a is shown in Fig. 2b. It is clear that the bulk laminarity is a superposition of stacked lamina on the nanoscale. Examination of numerous AFM images similar to Fig. 2b for this and other nanocomposites of the series, shows that the average undulation observed in each AFM image is $\sim$60 nm.

Figure 3a shows the X-ray diffraction patterns of both the $(CdCl_2)_y(C_nH_{2n+4}N)$ and $(CdS)_x(CdCl_2)_y(C_nH_{2n+4}N)_z$ series of nanocomposites. The $\{00l\}$ reflections observed in patterns **1** and **2** of the $(CdCl_2)_y(C_nH_{2n+4}N)$ series are evidence of the formation of a crystalline matrix. The degree of laminar crystallinity is reflected by the observation of eighth order $\{00l\}$ reflections for these compounds. The reflection intensities and double angle position have a close correlation to that of pure $CdCl_2$ (JPDS 01-0169). The additional reflections are due to the composites other constituents: surfactant molecular array and the concomitant formation of CdS. The synthesis, however, does not contain pure $CdCl_2$ nor pure CdS. The reflections observed are related to the partial substitution of the S^{2-} anion by the Cl^- anions, forming the $CdCl_2$ compound. The interlaminar distance for the $\{00l\}$ reflections, however, must consider the resident intercalated surfactant. For the whole $(CdS)_x(CdCl_2)_y(C_nH_{2n+4}N)_z$ series of nanocomposites in this work, we observe the presence of two crystalline lamellar phases. From Fig. 3b, the nanocomposites are composed of two principal interlaminar spacings: the $(CdS)_x(CdCl_2)_y$ lamina with d_{lam} $\sim$3.26 nm (**i**) and the second with d_{lam} of $\sim$2.69 nm (**ii**).

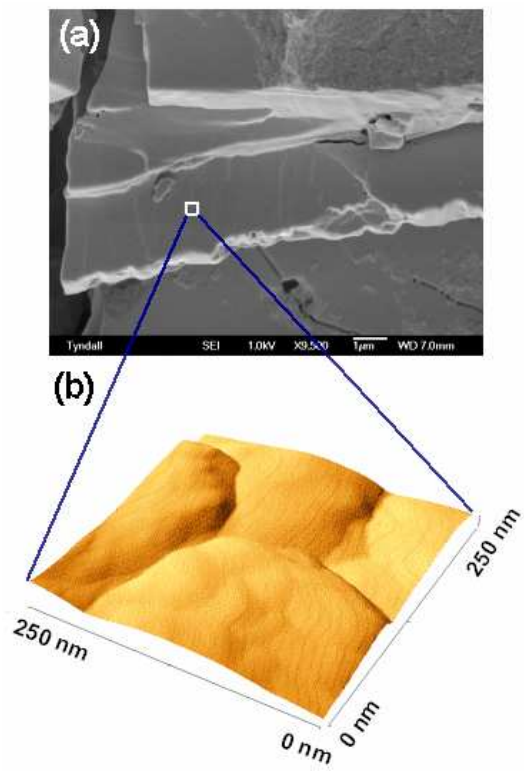

Fig. 2. (a) SEM image of the CdS_x-CTAB (75-100) and (b) corresponding 250 nm $\times$ 250 nm AFM image of the surface parallel to the nominal direction of laminarity.

These are the interlaminar distances (d_{lam}) for the overall interlaminar spacing of the nanocomposite and that of the interlaminar length of the surfactant, respectively [18]. The slight reduction in length of the interlaminar surfactant from 2.79 nm (see Fig. 3b) to 2.69 nm is due to both angled ordering within the lamina and overlapping of adjacent alkyl chains.

For the nanocomposites synthesised with the CTAB surfactant template, the interlamellar distances are in the range 0.30−0.36 nm. This series exhibit a high degree of crystallinity evidenced by the observation of fifth order $\{00l\}$ reflections in their respective X-ray patterns with an increase of 0.4 nm with respect to the pure ammonium salt which has an interlaminar distance of ∼2.8 nm [19]. Nanocomposites synthesised with OTAB, on the other hand, tend to have interlaminar distances of ∼3 nm with little variation but do exhibit stronger reflection intensities from the high crystallinity $(CdS)_x(CdCl_2)_y$ layers and comparatively negligible contributions at higher double angles, seen in patterns **2** and **7** in Fig. 3a, for example. The reflections in the higher angular range $2\theta = 20 - 22°$ are those of the alkyl chains that arise from the ordered interlaminar arrangement of the CTAB or OTAB surfactant.

For the $(CdS)_x(CdCl_2)_y(C_nH_{2n+4}N)_z$ series of nanocomposites we observe a quasi-linear relationship between the quantity of CTAB surfactant and the measured interlamellar distance, d_{lam}. In the case of nanocomposites synthe-

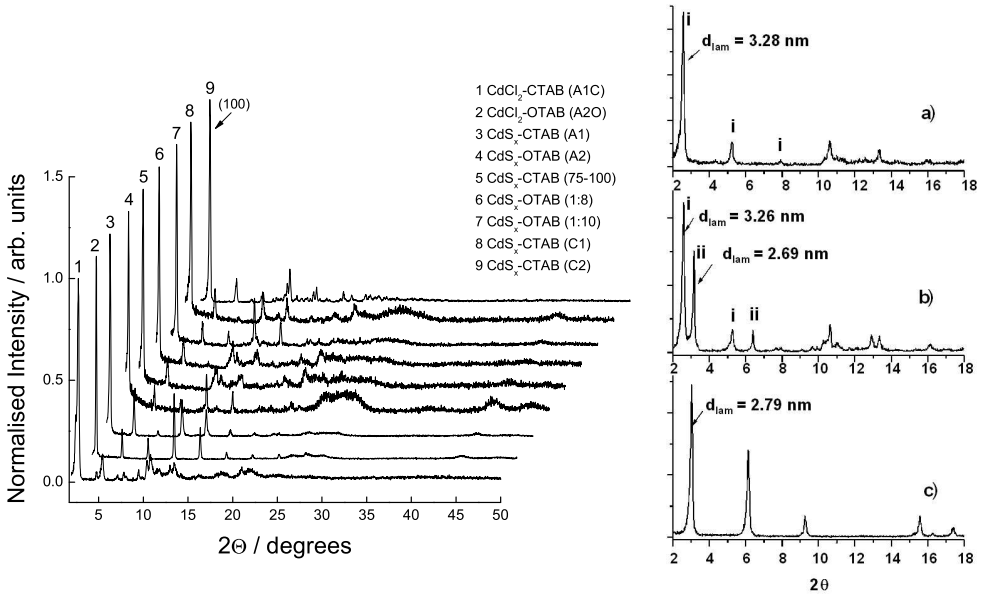

Fig. 3. (*Left*) X-ray diffraction patterns of the $(CdS)_x(CdCl_2)_y(C_nH_{2n+4}N)_z$ series of nanocomposites. Eighth order $\{00l\}$ planes were observed. (*Right*) XRD patterns of (a) $(CdS)_x(CdCl_2)_y$(OTAB) (b) $CdCl_2$(OTAB) (c) OTAB are also shown evidencing the two principal series of interlaminar spacings. Contributions from the intercalated surfactant are principally observed at $2\theta > 20$ degrees.

sised with OTAB, d_{lam} is marginally greater in all cases and exhibits a non-linear relationship with the OTAB concentration. Details on the interlaminar distances, d_{lam}, for all the nanocomposites can be found in Table 2.

Based on the detailed XRD and SEM measurements, and taking into consideration details of the organic surfactant, a simplistic schematic model of the system is presented in Fig. 4. The surfactant acts as the interlaminar binding template for the $(CdS)_x(CdCl_2)_y$ layers. The formation of the lamellar $CdCl_2$-surfactant complex can be understood by considering the presence of weak interactions during self-assembly between the surfactant and the inorganic precursor in the nanocomposite. These interactions favour the formation of the lamellar structure, resulting in electrostatic interactions between the inorganic precursor ($CdCl_2$) and the surfactant. A detailed report on the intercalation mechanism for this system, however, will be published elsewhere [20].

The X-ray diffraction patterns show evidence for a uniform and ordered solid, where the surfactant acts as a structural director defining the laminarity of the product. The reflections of the X-ray patterns at low 2θ angles do not correspond to pure cadmium sulphide. Identification of the phase shows that it corresponds to the greenockite structure (PDF 41−41049) where the structure consists of stacked SCd_4 tetrahedrons. The tetrahedrons are all oriented in one direction and produce the hexagonal (six-fold rotational) symmetry.

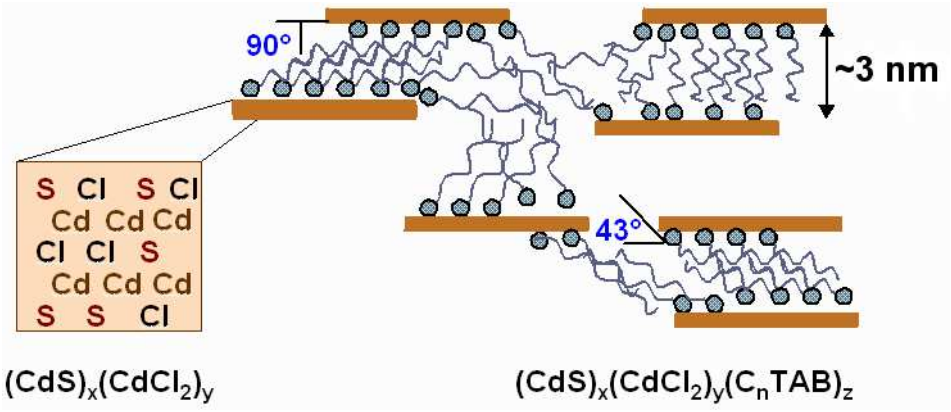

Fig. 4. Schematic representation of the surfactant-intercalated lamellar nanocomposite structure.

TEM was employed to examine the microstructural nature of the nanocomposite. Part of the nanocomposite can be seen in Fig. 5 which are a pair of bright and dark field images.

The region shown demonstrates the presence of thin platelets **A** that vary in width from ∼50−150 nm and ∼600−700 nm in length. Such platelets are clearly mono-crystalline as indicated by the form of the contrast seen in the dark field image shown in Fig. 5b and can be compared with the rectangular and cube shaped particles marked at **B** and **C** respectively as well as the much finer grained material marked at **D**. The grain size of the nanoparticles located in the latter area **D** is ∼10 nm. Electron diffraction was employed to clarify the composition of the nanocomposite. The inset to Fig. 5b shows the diffraction pattern obtained. The spacings of the rings marked at **1**−**6** in the diffraction pattern and associated indexation are given in Table 1. A close correlation can be made with the spacings of the hexagonal CdS phase (Space Group: P63mc) for which $a_0 = 0.4142$ nm and $c_0 = 0.6724$ nm.

Ring ID	$d-$spacing (nm)	Indexation $\{hkl\}$
1	0.3546	(100)
2	0.3388	(002)
3	0.3210	(101)
4	0.2103	(110)
5	0.1906	(103)
6	0.1768	(112)

Table 1
Indexation of the selected area electron diffraction pattern of the CdS_x-CTAB (C2) nanocomposite from Fig. 5b.

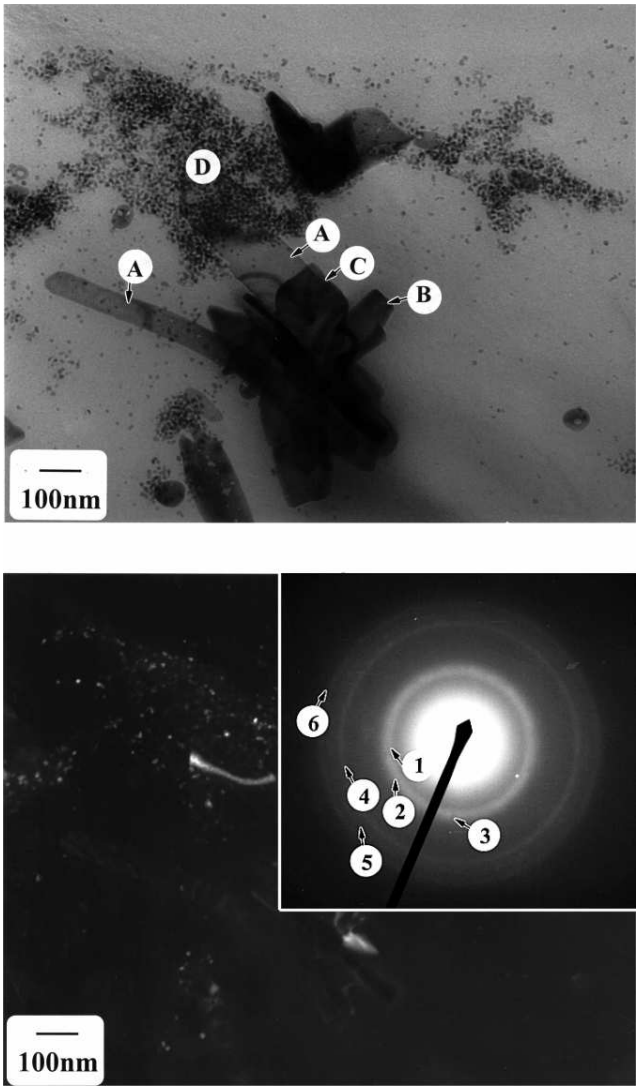

Fig. 5. Bright field (upper) and corresponding dark field (lower) TEM images of the CdS_x-CTAB (C2) nanocomposite. (*inset*) Associated selected area electron diffraction pattern. Each of the constituent diffraction rings are marked **1**−**6**.

3.2 Diffuse Reflectance Measurements

The optical properties of the $(CdS)_x(CdCl_2)_y(C_nH_{2n+4}N)_z$ series were estimated using UV-VIS diffuse reflectance spectra. The compounds exhibit a strong absorption in the visible range, as well this series present changes when the concentration of CdS changes. The optical absorption of the nanocomposites plotted in Fig. 6 according to the Kubelka-Munk remission function [21–23] from the diffuse reflectance spectra at constant scattering:

$$\frac{k}{S} = \frac{(1 - R_d)^2}{2R_d}, \tag{2}$$

where k is the absorption coefficient, S the scattering coefficient, and R_d the diffuse reflectance. The S is typically much less dependent on photon energy ($h\nu$) than k around the band edge and thus can be regarded as being almost constant. Therefore, the $h\nu$ dependence of k/S is generally considered to show the optical absorption spectrum of the sample [24]. From Fig. 6, the direct band-gap absorption edge is estimated for a series of $(CdS)_x(CdCl_2)_y(C_nH_{2n+4}N)_z$ nanocomposites.

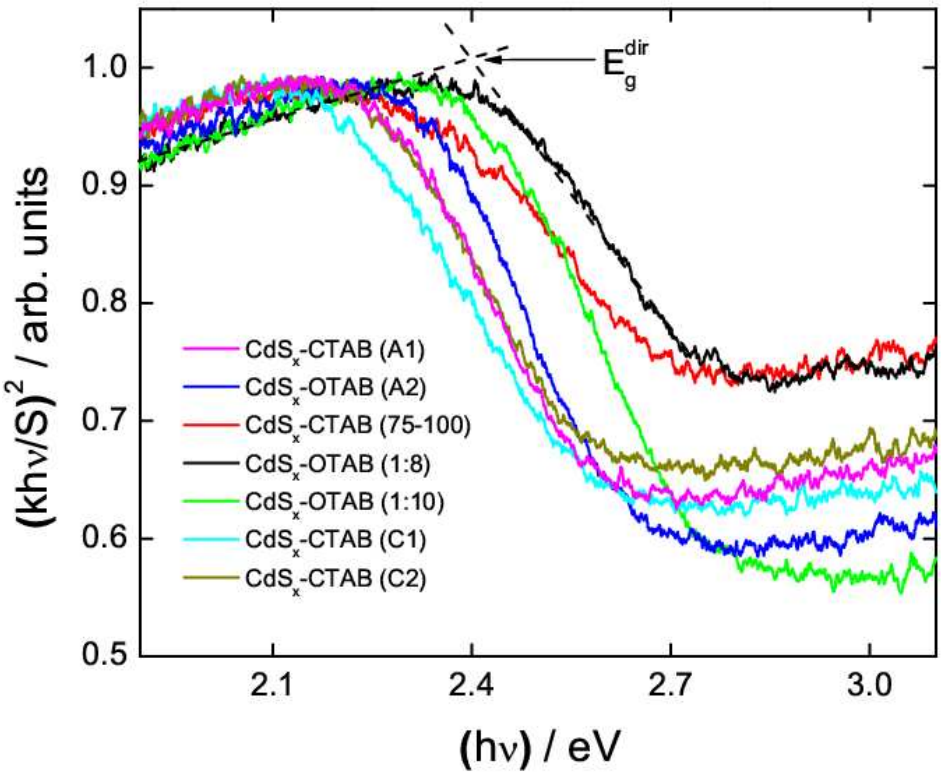

Fig. 6. Kubelka-Munk curves obtained from diffuse reflection measurements of several $(CdS)_x(CdCl_2)_y(C_nH_{2n+4}N)_z$ nanocomposites. The value on the abscissa corresponding to the intercept of the marked best-fit trends indicates the direct band-gap energy.

From Fig. 6, the direct band-gap energies for all nanocomposites studied were estimated. The measured bang-gap energies are in the range 2.11−2.40 eV with corresponding absorption edges of 517−588 nm. Further details can be found in Table 2 for the entire series of nanocomposites. These values are red-shifted when compared with the known bulk confined electronic transition in CdS of 2.45 eV and thus quantum confinement effects [26] do not explain the nature of emission processes within the nanocomposite.

3.3 Photoluminescence Excitation Spectroscopy

The PLE spectra for the CdS_x-CTAB (75-100) nanocomposite at a range of incident radiation powers is shown in Fig. 7. The maximum of emission is observed at ∼670 nm with the normalized intensity increasing with increasing incident laser power. The presence of a distinct satellite shoulder peak is observed in all spectra and scales with the main emission peak. Excitation by lower energy radiation results in a band-narrowing and blue-shifting of the main emission and a marked increase in the intensity of the satellite shoulder peak. The emission spectrum of CdS typically exhibits emission variations as a function of nanoparticle size and due to their surface states [28].

The prominent shoulder peak at 615 nm is attributed to emission from decay of trap levels located 0.14 eV below the conduction band of the CdS_x-CTAB (75-100) nanocomposite, in Fig. 7. It is also observed not to be red- or blue-shifted when the incident probing radiation wavelength is changed. Such levels are associated with doubly ionised sulphur vacancies, V_S^{2+} [29] and most often observed in cadmium-rich crystals with added chlorine dopants [30]. Thus, the presence of the shoulder peaks is due to the self-assembled laminar crystalline array of Cd, S and Cl forming the broad-band luminescent structure.

The observed band gap energy from Fig. 7 does not correlate with neither the bulk confined electronic transition of CdS (2.45 eV) nor with the optical transition energy of small, quantum-confined CdS nanocrystal quantum dots. The typical recombination process observed in these composites is much different to what is known for CdS-like materials as its emission does not show signatures of CdS excitons such as the well documented $1_{S_e} - 1_{S_h}$ transition [31,32] typically observed at ∼495 nm [28].

The absorption edge determined from PLE measurements is observed in the range 520−560 nm for the three nanocomposites shown in Fig. 8. The absorption edge values, overall, range from 520−590 for the entire series of nanocomposites and varies in accordance with the values determined by diffuse reflectance spectroscopy in Fig. 6. The data is sumarised in Table 2. Since the PLE directly reflects the density of absorbing states, Fig. 8 shows that the absorption seems to be governed by CdS bulk electronic states. The relatively large red-shift of the emission is due to an energetic relaxation charge carriers (holes) into defect levels of a yet unknown kind. The emission in the red spectral range is not due to a confined state of CdS, which would have to be at shorter wavelength.

The principal emission is noted to be red-shifted to that of bulk CdS and to depend on both excitation energy and the mole fraction of CdS in the intercalate relative to the Cd^{2+} containing centers. Fig. 9a highlights the intention

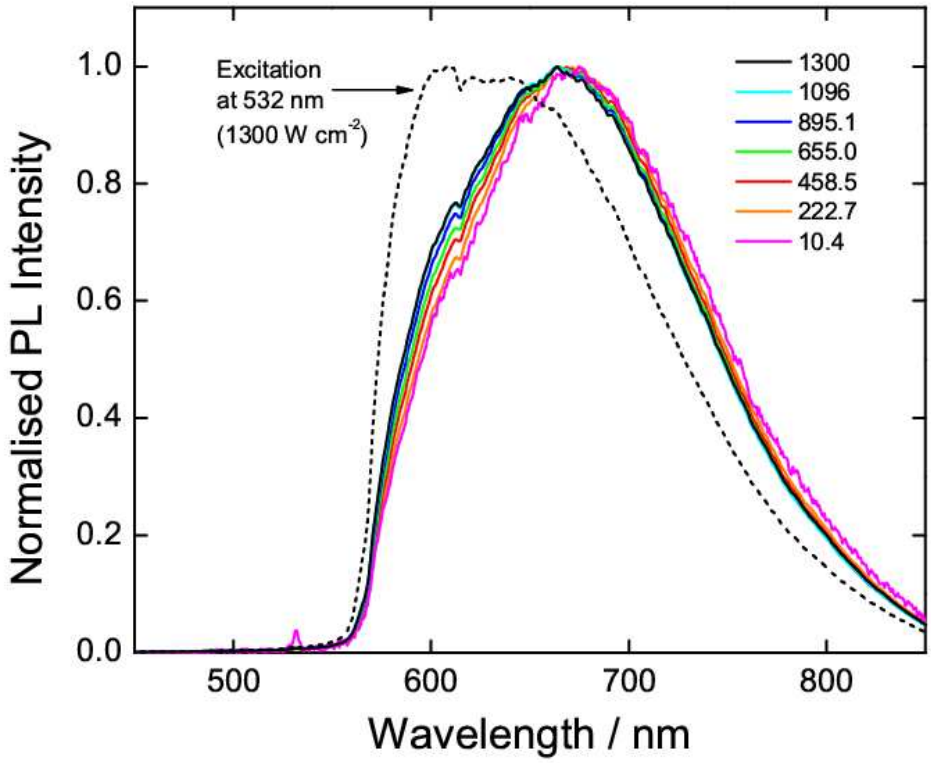

Fig. 7. Photoluminescence spectra of the CdS_x-CTAB (75-100) nanocomposite at an excitation wavelength of 409 nm between applied power densities in the range 10−1300 W cm^{-2} at room temperature. The overlaid spectrum is that of the CdS_x-CTAB (75-100) at an excitation wavelength of 532 nm normalized to its own photon flux.

of the synthesis by showing the variation of the measured band-gap energy as a function of the mole fraction of CdS and $CdCl_2$ for the nanocomposites.

As the mole fraction of CdS increases (i.e. the nominal-flow concentration of H_2S is increased), the peak intensity of the band-gap emission shifts to higher values (lower energy) with a corresponding increase in absolute intensity observed. Similar observations have been reported for co-precipitated CdS-CdSe core-shell nanoparticles upon the addition of H_2S:H_2Se gases [27]. The band-gap energy, E_g^{dir}, is also observed (Fig. 9b) to vary quasi-linearly with the nominal $CdCl_2$ mole fraction in each of the nanocomposites. In Fig. 9c, we observe that the interlaminar distance d_{lam}, increases with greater mole fraction of CdS. Furthremore, d_{lam} shows a similar decrease for both the mole fraction of CdS and the mole fraction ratio of CdS:$CdCl_2$, indicating that the greater molar volume of $CdCl_2$ is contributes to the wider interlaminar distance.

We note E_g^{dir} to decrease slightly with decreasing mole fraction of CdS, however, a marked decrease is observed at much lower CdS mole fractions. Pre-

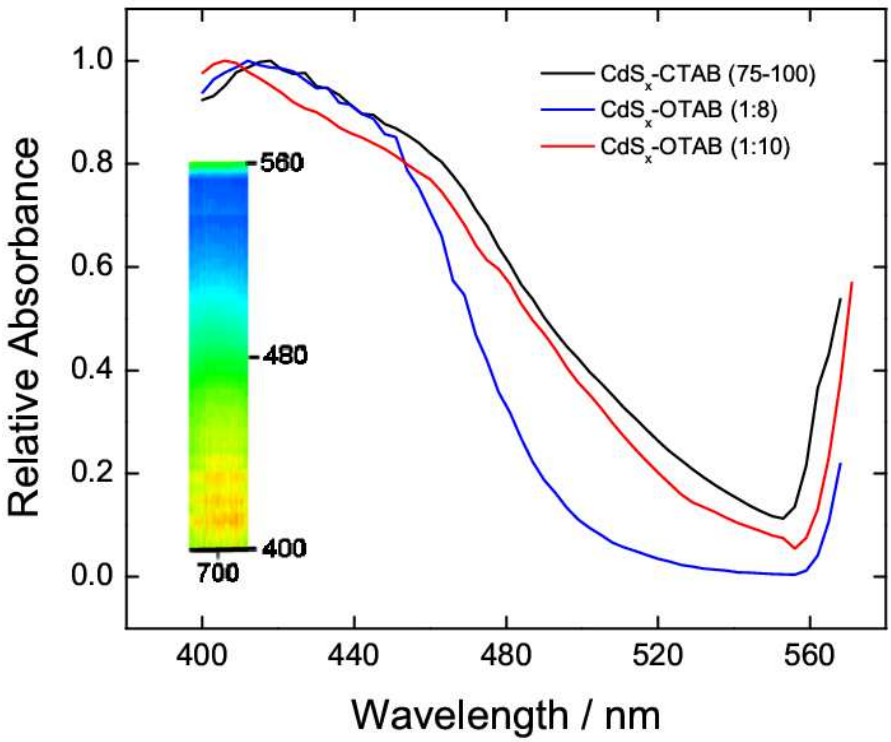

Fig. 8. Relative absorption spectra for several $(CdS)_x(CdCl_2)_y(C_nH_{2n+4}N)_z$ nanocomposites at excitation wavelengths in the range 400−560 nm. (*inset*) Corresponding 2D relative absorption map at excitation wavelengths in the range 400−560 nm for the CdS_x-CTAB (75-100) nanocomposite detected from 650−750 nm.

vious observations with other CdS-containing compounds [27,28,16,17] have attributed the broad-band emission they observed at ∼670 nm to the recombination of trapped carriers (holes). Cadmium ions (Cd^{2+}) are known to activate the excitonic emission of colloidal CdS particles in a highly media-dependent fashion [33]. In this work the tendency in all cases is to form solid $CdCl_2$ with the concomitant formation of CdS regions under gaseous H_2S flow. Since Cd^{2+} ions are activators of excitonic emission in CdS nanocrystals, their double-quantity uptake by the Cl^- ions depletes the amount available for activation of CdS emission, thus we observe a marked decrease in E_g^{dir} at high mole fraction ratios in Fig. 9c. Thus, we see evidence for the activation of colloidal-like CdS regions within the nanocomposites due to the presence of cadmium ions in excess. Shifting of E_g^{dir} is directly related to the formation of CdS within the nanocomposite with cadmium ions in excess and is noted to be considerable at mole fraction ratios >0.5. Irrespective of the synthetic method of preparation, once the ratio of nominal mole fraction of CdS to $CdCl_2$ remains relatively unchanged for each nanocomposite, the wavelength of the peak intensity from PLE measurements remained invariant.

The time-resolved PL emission of the CdS_x-CTAB (75-100) nanocomposite

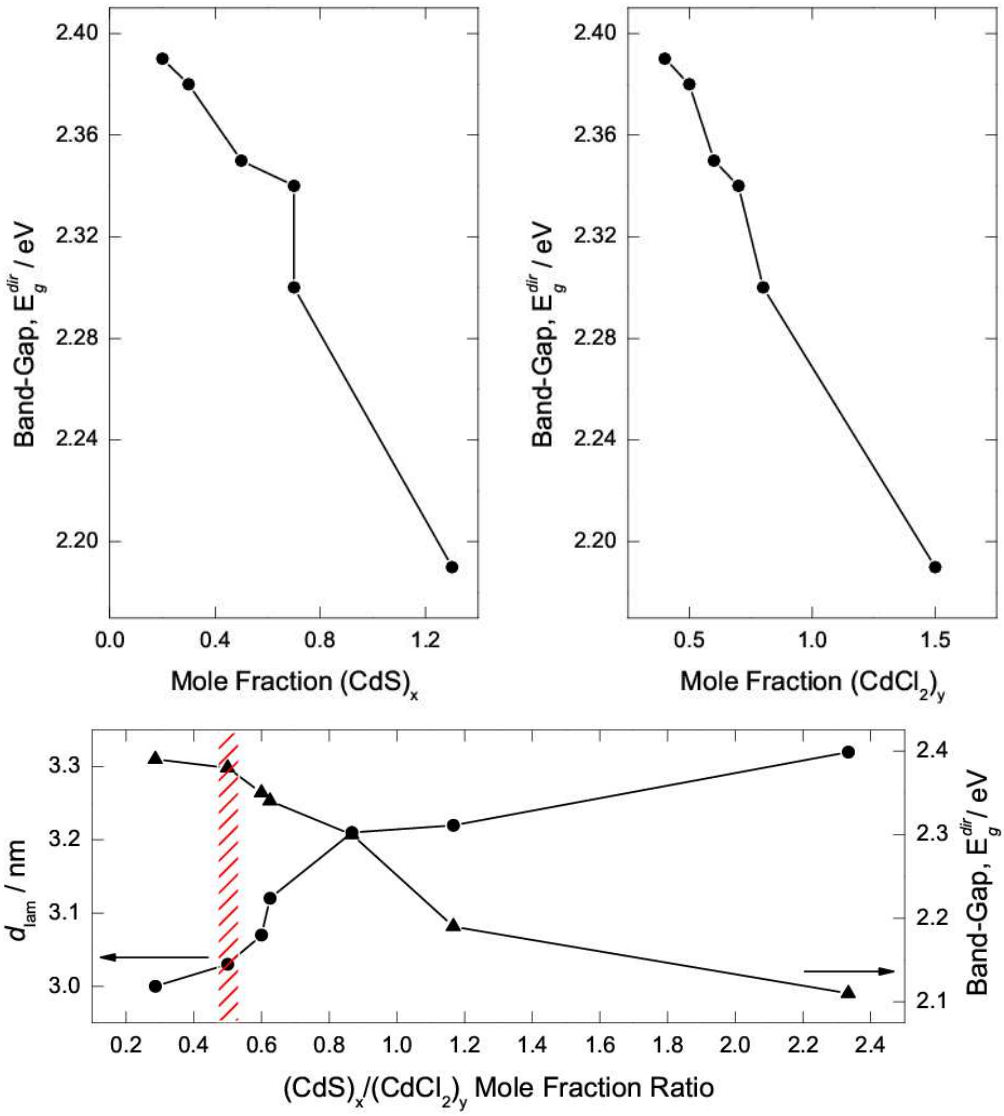

Fig. 9. Variation of the measured band-gap energy of the $CdS)_x(CdCl_2)_y(C_nH_{2n+4}N)_z$ nanocomposites as a function of the mole fractions of (a) CdS and (b) $CdCl_2$. (c) Dependence of the measured band-gap energy -▲- and the interlaminar distance, d_{lam} -●-, on the mole fraction ratio of $(CdS)_x$:$(CdCl_2)_y$. The marked area indicates equivalent mole fractions of CdS and $CdCl_2$.

is shown in Fig. 10. The decay is homogeneous over the full emission range (640−740 nm) with only minor changes. All time-resolved PL decay curves were found to be multi-exponential in profile which is indicative of systems with highly dispersed trap energy levels [34].

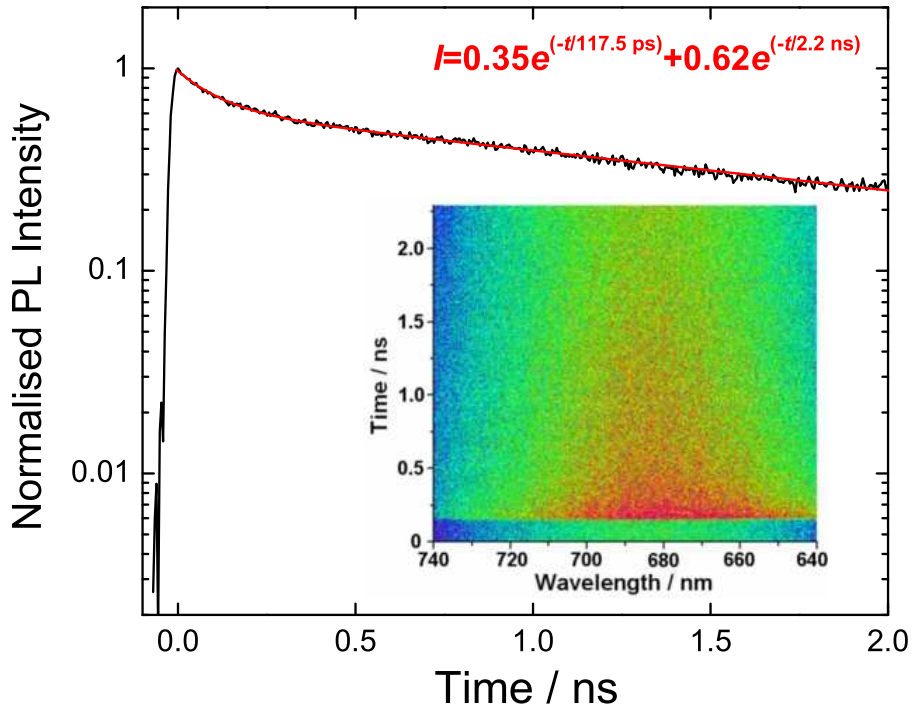

Fig. 10. Time-resolved photoluminescence spectrum of the CdS_x-CTAB (75-100) nanocomposite under cw excitation at 532 nm. The insert shows the spectrally resolved 2D TRPL map over the detection wavelength range 640−740 nm.

4 Conclusions

Each of the nanocomposites have a unique variation in synthesis procedure, but all result in a powder solid. X-ray diffraction measurements of the nanocomposites exhibited interlaminar distances in the range 0.29−0.36 nm with observations of eighth order $\{00l\}$ diffraction planes indicative of a high degree of laminarity and crystallographic order. Diffuse reflectance measurements have determined that the profile of their emission spectrum is that of a direct band-gap with absorption edges in the range 2.11−2.40 eV, depending on the CdS mole fraction in the nanocomposite. Photoluminescence (PL) excitation spectroscopy shows the main emission to be at ∼670 nm; the maximum and minimum of relative absorbance are observed at 420 nm and 560 nm, respectively. We did not observe any excitonic emission from the $(CdS)_x(CdCl_2)_y(C_nH_{2n+4}N)_z$ series of nanocomposites. The electronic states inside of the lamellar nanocomposite are governed by optical properties of bulk CdS. The absorption occurs in continuum states of CdS. The excited charged carriers then relax into defect states formed by structural defects in

Nanocomposite	d_{lam} (nm)	Band-Gap (eV)	λ_{abs} (nm)	Optical Gap
$CdCl_2$-CTAB (A1C)	2.96	–	–	–
$CdCl_2$-OTAB (A2O)	3.65	–	–	–
CdS_x-CTAB (A1)	3.00	2.23	567	Direct
CdS_x-OTAB (A2)	3.12	2.29	542	Direct
CdS_x-CTAB (75-100)	3.03	2.26	549	Direct
CdS_x-OTAB (1:8)	3.21	2.40	517	Direct
CdS_x-OTAB (1:10)	3.22	2.37	523	Direct
CdS_x-CTAB (C1)	3.07	2.19	566	Direct
CdS_x-CTAB (C2)	3.32	2.11	588	Direct

Table 2
Details of the nanocomposites, band-gap energies determined by DRS, XRD measurements of the interlaminar distance d_{lam}, the absorption edge wavelength λ_{abs}, and the optical band-gap type for the $(CdS)_x(CdCl_2)_y(C_nH_{2n+4}N)_z$ series of nanocomposites.

the nanocomposites such as doubly ionized sulphur vacancies (V_S^{2+}) in the Cd-rich layers.

Development of a system that allows the investigation of subtle surface-state interactions and reactions resulting in band-gap tunable nanocomposites has been presented. It opens the door to investigations of surfactant-mediated laminar CdS nanocomposites from fundamental electronic and optical transitions to band-gap engineering via a simple chemical synthesis route.

Acknowledgements

The support of the Science Foundation Ireland (SFI) under Investigator Award 02/IN.1/172 and FONDECyT (Grants 1050344, 1030102, 7050081) are gratefully acknowledged. The support of the EC-funded projects P*h*OREMOST (FP6/2003/IST/2-511616) is gratefully acknowledged.

References

[1] D. Routkevitch, T. Bigioni, M. Moskovits, J. M. Xu, J. Phys. Rev. 100 (1996) 14037.

[2] I. P. Silva Filho, J. C. O. Santos, M. M. Conceição, L. M. Nunes, I. M. G. Santos, A. G. Souza, Mater. Lett. 19-20 (2005) 2510.

[3] S. R. Forrest, Nature (London) 428 (2004) 911.

[4] A. L. Efros, A. L. Efros, Sov. Phys. Semicond. 16 (1982) 772.

[5] P. Zhang, L. Gao, J. Coll. Inter. Sci. 266 (2003) 457.

[6] H. Zhang, D. Yang, X. Ma, Y. Ji, S. Li, D. Que, Mater. Chem. Phys. 93 (2005) 65.

[7] N. Mirabal, V. Lavayen, E. Benavente, M. A. Santa Ana, G. González, Microelectronics Journal 35 (2004) 37.

[8] W. Chen, Y. Xu, Z. Lin, Z. Wang, L. Lin, Solid State Commun. 105 (1998) 129.

[9] C. Yang, D. D. Awschalom, G. Stucky, Chem. Mater. 14 (2002) 1277.

[10] V. Bekiari, P. Lianos, Langmuir 16 (2000) 3561.

[11] E. D. Sone, E. R. Zubarev, S. L Stupp, Small 1 (2005) 694.

[12] E. D. Sone, E. R. Zubarev, S. L. Stupp, Angew. Chem. 144 (2002) 1781.

[13] C. B. Murray, D. J. Norris, M. G. Bawendi, J. Am. Chem. Soc. 115 (1993) 8706.

[14] N. Gaponik, D. V. Talapin, A. L. Rogach, K. Hoppe, E. V. Shevchenko, A. Kornowski, A. Eychmüller, H. Weller, J. Phys. Chem. B 106 (2002) 7177.

[15] A. L. Rogach, D. V. Talapin, H. Weller, Colloids and Colloid Assemblies 52 (2004).

[16] H. Weller, Adv. Mater. 5 (1993) 88.

[17] H. Weller, Angew. Chem. Int. Ed. 32 (1993) 41.

[18] J. Y. Ying, A. Nakahira, D. M. Antonelli, Inorg. Chem. 35 (1996) 3126.

[19] B. Messer, J. Hee, M. Huang, Y. Wu, F. Kim, P. Yan, Adv. Mater. 12 (2000) 1526.

[20] N. Mirabal, V. Lavayen, M. A. Santa Ana, E. Benavente, S. Ormazabal, C. M. Sotomayor Torres, G. González, (unpublished).

[21] P. Kubelka, F. Munk, Z. Techn. Physik. 12 (1931) 593.

[22] G. Pang, S. Chen, Y. Koltypin, A. Zaban, S. Feng, A. Gedanken, Nano Lett. 1 (2001) 723.

[23] T. Umebayashi, T. Yamaki, H. Itoh, K. Asai, Appl. Phys. Lett. 81 (2002) 454.

[24] B. M. Weckhuysen, R. A. Sehoonheydt, Catal. Today 49 (1999) 441.

[25] T. Nakamura, T. Suemasu, K. Takakura, F. Hasegawa, A. Wakahara, M. Imai, Appl. Phys. Lett. 81 (2002) 1032.

[26] R. Rossetti, R. Huli, J. M. Gibson, L. E. Brus, J. Chem. Phys. 82 (1985) 552.

[27] T. Tian, T. Newton, N. A. Kotov, D. M. Guldi, J. H. Fendler, J. Phys. Chem. 100 (1996) 8927.

[28] T. Tian, C. Wu, J. H. Fendler, J. Phys. Chem. 98 (1994) 4913.

[29] K. H. Nicholas, J. Woods, Brit. J. Appl. Phys. 15 (1964) 783.

[30] J. Woods, K. H. Nicholas, Brit. J. Appl. Phys. 15 (1964) 1361.

[31] L. Spanhel, M. Haase, H. Weller, A. Henglein, J. Am. Chem. Soc. 109 (1987) 5649.

[32] L. Spanhel, H. Weller, A. Henglein, J. Am. Chem. Soc. 109 (1987) 6632.

[33] A. Eychmüller, A. Hässelbarth, L. Katsikas, H. Weller, Ber. Bunsenges Phys. Chem. 95 (1991) 79.

[34] A. Eychmüller, A. Hässelbarth, L. Katsikas, H. Weller, J. Lumin. 48/49 (1991) 745.